Free and forced response of three-dimensional waveguides with rotationally symmetric cross-sections

Fabien Treyssède

Free and forced response of three-dimensional waveguides with rotationally symmetric cross-sections

Fabien Treyssède[a,*],

[a]*IFSTTAR, GERS, GeoEND, F-44344, Bouguenais, France*

Abstract

The analysis of high-frequency wave propagation in waveguides of arbitrarily shaped cross-sections requires specific numerical methods. A rather common technique consists in discretizing the cross-section with finite elements while describing analytically the axis direction of the waveguide. This technique enables to account for the continuous translational invariance of a waveguide and leads to a modal problem written on the cross-section. Although two-dimensional, solving the so-obtained eigensystem can yet become computationally costly with the increase of the size of the problem. In most applications involving waveguides, the cross-section itself often obeys rules of symmetry, which could also be exploited in order to further reduce the size of the modal problem. A widely encountered type of symmetry is rotational symmetry. Typical examples are bars of polygon-shaped cross-section or multiwire cables. The goal of this paper is to propose a numerical method that exploits the discrete rotational symmetry of the waveguide cross-section. Bloch-Floquet conditions are applied in the circumferential direction while the continuous translational invariance of the waveguide along its axis is still described analytically. Both the free and the forced response problems are considered. A biorthogonality relationship specific to the rotationally symmetric formulation is derived. Numerical results are computed and validated for the simple example of a cylinder and for the more complex test case of a multiwire structure. In addition to reducing the computational effort, the rotationally symmetric formulation naturally provides a classification of modes in terms of their circumferential order, which can be of great help for the dynamic analysis of complex structures.

Keywords: wave ; finite element ; rotational symmetry ; mode ; response ; cable

1. Introduction

Elastic guided waves are of great interest for the dynamic analysis of elongated structures and provide the theoretical background necessary for many applications (nondestructive evaluation, vibration and noise reduction, statistical energy analysis...). Guided waves are yet multimodal and dispersive. Modeling tools are required to further understand the mechanism of their propagation. Dispersion curves of phase and group velocities as functions of frequency typically enable to identify modes that propagate in a frequency range of interest. Such curves represent modal properties obtained regardless excitation (free response). It is also essential to determine and control the amplitudes of each guided modes excited by a given source (forced response). This can be investigated with the help of modal excitabilities [1, 2] (for a given frequency, the excitability of a mode is defined as the ratio of the displacement of that mode to a point force applied in a given direction).

Canonical geometries (plates, cylinders) can be modeled thanks to analytical methods, such as the Thomson-Haskell [3, 4], the stiffness matrix [5] or the global matrix [6] methods. However, the analysis of arbitrarily shaped three-dimensional waveguides requires numerical methods.

Based on the theory of wave propagation in periodic structures, a first numerical approach consists in applying boundary conditions based on Floquet's principle in the finite element (FE) model of a single repetitive cell of the

*Corresponding author
Email address: fabien.treyssede@ifsttar.fr (Fabien Treyssède)

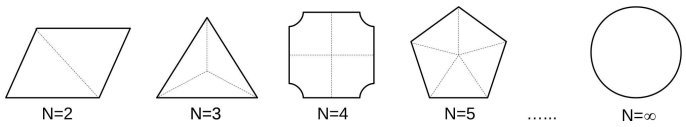

Figure 1: Examples of rotationally symmetric cross-sections (N denotes the order of rotational symmetry)

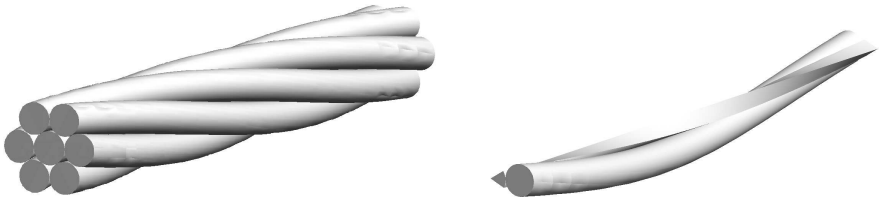

Figure 2: Example of a multi-wire cable: (a) three-dimensional geometry of a seven-wire strand, (b) unit cell view ($N = 6$).

problem (see Refs. [7, 8, 9, 10] for instance). This first approach leads to a modal problem, three-dimensional but reduced on the unit cell. When the translational invariance of the waveguide is continuous, another technique consists in discretizing only the cross-section of the waveguide while describing analytically the direction of wave propagation. Compared to the first approach, this second method also leads to a modal problem but the problem is reduced on the cross-section (two-dimensional), which further reduces the computational cost. This second approach, which will be termed as *waveguide formulation* in this paper, has been applied under various names in the literature: the extended Ritz technique, the thin layer method for stratified waveguides in geophysics, the strip-element method, the semi-analytical finite element method or the scaled boundary finite element method in ultrasonics (see *e.g.* Refs. [11, 12, 13, 14, 15, 16]).

Although two-dimensional, the eigenproblem of the waveguide formulation can still be computationally costly when the FE mesh has to be refined and/or the modal density increases (*e.g.* at high frequency [17]). It is hence desirable to further reduce the size of the modal problem. The goal of this paper is to propose a waveguide formulation that accounts for the rotational symmetry of cross-sections. With a modal approach, accounting for rotational symmetry has indeed two computational benefits: the reduction of the problem size in terms of degrees of freedom and the reduction of the number of modes to compute.

Rotationally symmetric cross-sections are often encountered in practical applications (for instance, regular polygons). Simple examples are given by Fig. 1 for various orders of rotational symmetry, denoted by N in this paper. Another example is that of multi-wire cables, for which the modeling is of particular interest in the context of non-destructive evaluation. Cables are usually made of individual helical wires, which are coupled through contact conditions. As an example widely employed in civil engineering cables, Fig. 2 depicts a seven-wire strand, constituted by a central cylindrical wire surrounded by six helical wires (here, the order of rotational symmetry is hence equal to 6). Such a structure yields large size problems involving mesh refinements in the contact regions [18].

Investigating the free response of three-dimensional waveguides, the first approach has been applied in Ref. [19] by revising the Bloch-Floquet conditions in order to consider discrete symmetries that are not purely translational, including screw and rotational symmetries. The particular case of continuous rotational symmetry, *i.e.* axisymmetric waveguides (pipes and cylinders), has been treated in the literature using both the first approach [20, 21] and the second approach [22, 23]. Among these references, the forced response has been investigated in Refs. [21, 22] only. Regardless waveguides, the structural modeling of discrete rotational symmetry has also been explored in the context of vibration analysis [24, 25]. In Refs. [20, 21, 19], it is noteworthy that Bloch-Floquet periodic boundary conditions are applied both in the axial and in the circumferential directions. Since the rotational symmetry of interest in this paper is of discrete type, the cross-section of the waveguide has to be viewed as a periodic medium along the circumferential direction. Hence, the circumferential periodic conditions used in the present paper are of Bloch-Floquet type also. However, the propagation along the waveguide axis is still described analytically in order to fully exploit the continuous translational symmetry of the waveguide along its axis.

Section 2 briefly recalls the waveguide formulation for arbitrarily shaped cross-sections. The rotationally symmet-

ric formulation is presented in Sec. 3 by treating both the free and the forced response problems. The forced response is solved by expanding the excited field as a sum of the guided modes determined from the free response. One difficulty is that the introduction of rotational symmetry in the waveguide formulation breaks the symmetry property of the eigenproblem. A specific biorthogonality relationship between eigenmodes is hence derived to determine the contribution of each mode explicitly as a function of the excitation. Sections 4 and 5 are devoted to numerical results. In Sec. 4, a cylindrical waveguide of circular cross-section is considered to validate the approach. Section 5 shows results obtained for a seven-wire strand and demonstrates the potentiality of the method.

2. Background: waveguide formulation

The waveguide formulation is a FE method dedicated to waveguides that aims to account for the translational invariance of the geometry to reduce the size of the problem. The initial fully three-dimensional problem is reduced to a two-dimensional modal problem so that one only needs to mesh with FE the cross-section of the waveguide. This section briefly recalls the waveguide formulation. Details can be found in the literature (see *e.g.* [14, 15]).

Let us denote (x, y) the cross-section coordinates and z the axis coordinate of the waveguide. First, the strain-displacement relation is written as:

$$\boldsymbol{\epsilon} = (\mathbf{L}_{xy} + \mathbf{L}_z \partial/\partial z)\mathbf{u} \tag{1}$$

where $\mathbf{u}$ denotes the displacement field, $\mathbf{L}_{xy}$ is the operator containing all terms but derivatives with respect to the z-axis and $\mathbf{L}_z$ is the operator of z-derivatives:

$$\mathbf{L}_{xy} = \begin{bmatrix} \partial/\partial x & 0 & 0 \\ 0 & \partial/\partial y & 0 \\ 0 & 0 & 0 \\ \partial/\partial y & \partial/\partial x & 0 \\ 0 & 0 & \partial/\partial x \\ 0 & 0 & \partial/\partial y \end{bmatrix}, \quad \mathbf{L}_z = \begin{bmatrix} 0 & 0 & 0 \\ 0 & 0 & 0 \\ 0 & 0 & 1 \\ 0 & 0 & 0 \\ 1 & 0 & 0 \\ 0 & 1 & 0 \end{bmatrix}. \tag{2}$$

After applying a time Fourier transform, the approach consists in discretizing only the cross-section (x, y) by a FE method while describing analytically the direction of wave propagation z. Inside one finite element e, the displacement field can thus be expressed as follows:

$$\mathbf{u}(x, y, z, t) = \mathbf{N}^e(x, y)\mathbf{U}^e(z)e^{-\mathrm{i}\omega t} \tag{3}$$

where $\mathbf{U}^e$ is the nodal displacement vector, $\mathbf{N}^e$ is the matrix of nodal interpolating functions of the element e and ω is the angular frequency.

Following a waveguide formulation approach (see *e.g.* Refs. [22, 26] for details), the variational formulation of three-dimensional elastodynamics yields from Eqs. (1)–(3):

$$(\mathbf{K}_1 - \omega^2\mathbf{M})\mathbf{U} + (\mathbf{K}_2 - \mathbf{K}_2^{\mathrm{T}})\mathbf{U}_{,z} - \mathbf{K}_3\mathbf{U}_{,zz} = \mathbf{F} \tag{4}$$

with the elementary matrices:

$$\begin{aligned} \mathbf{K}_1^e &= \int_{S^e} \mathbf{N}^{e\mathrm{T}}\mathbf{L}_{xy}^{\mathrm{T}}\mathbf{C}\mathbf{L}_{xy}\mathbf{N}^e \mathrm{d}S, \quad \mathbf{K}_2^e = \int_{S^e} \mathbf{N}^{e\mathrm{T}}\mathbf{L}_{xy}^{\mathrm{T}}\mathbf{C}\mathbf{L}_z\mathbf{N}^e \mathrm{d}S, \\ \mathbf{K}_3^e &= \int_{S^e} \mathbf{N}^{e\mathrm{T}}\mathbf{L}_z^{\mathrm{T}}\mathbf{C}\mathbf{L}_z\mathbf{N}^e \mathrm{d}S, \quad \mathbf{M}^e = \int_{S^e} \rho\mathbf{N}^{e\mathrm{T}}\mathbf{N}^e \mathrm{d}S \end{aligned} \tag{5}$$

where $(\cdot)_{,z}$ denotes partial derivatives with respect to z, $\mathrm{d}S = \mathrm{d}x\mathrm{d}y$, $\mathbf{C}$ is the matrix of material properties and ρ is the mass density. For clarity, $\mathbf{U} = \mathbf{U}(z, \omega)$ is the column vector containing cross-section nodal displacements in the space-frequency domain. $\mathbf{F} = \mathbf{F}(z, \omega)$ represents the excitation vector in the space-frequency domain. For later use, it is also convenient to introduce the following vector:

$$\mathbf{T} = \mathbf{K}_2^{\mathrm{T}}\mathbf{U} + \mathbf{K}_3\mathbf{U}_{,z} \tag{6}$$

which can be interpreted as the nodal traction vector applied on the cross-section surface S of unit normal $\mathbf{e}_z$ [26].

Setting $\mathbf{F} = \mathbf{0}$ (no elastodynamic source) and performing a Fourier transform in the z direction (which is equivalent to introduce a space harmonic dependence e^{ikz}), Eq. (4) is a quadratic eigenvalue problem whose eigensolutions $\{k_m, \mathbf{U}_m\}$ are the guided modes propagating in the translationally invariant structure. Quadratic eigenproblems are more difficult to handle with standard numerical eigensolvers. A rather well-known procedure consists in recasting the quadratic eigenproblem as a linear one (see Refs. [27, 17] for instance). In this paper, the linear eigensystem is solved with the ARPACK library [28], appropriate for large sparse matrices and based on the implicitly restarted Arnoldi method.

One emphasizes that the matrices $\mathbf{K}_1$, $\mathbf{K}_3$ and $\mathbf{M}$ in Eq. (4) are symmetric and the matrix $(\mathbf{K}_2 - \mathbf{K}_2^{\mathrm{T}})$ is skew-symmetric. One consequence of these properties is that guides modes occur in pairs of opposite-going modes, denoted as $\{k_m, \mathbf{U}_m\}$ and $\{-k_m, \mathbf{U}_{-m}\}$. In this case, a biorthogonality relation involving opposite-going modes can be derived in order to calculate the forced response as a modal expansion on the guided modes. For waves travelling toward the positive z-direction and z outside the source region (one assumes that the excitation is zero outside a finite interval along z), the forced response can be expressed as follows [26]:

$$\mathbf{U} = \sum_{m>0} \mathbf{E}_m \hat{\mathbf{F}}(k_m) e^{ik_m z} \tag{7}$$

where $\mathbf{E}_m$ is the so-called modal excitability matrix:

$$\mathbf{E}_m = \frac{i\omega}{4Q_{m,-m}} \mathbf{U}_m \mathbf{U}_{-m}^{\mathrm{T}} \tag{8}$$

In Eq. (7), the summation is performed on positive-going waves only (denoted by positive values of m) and the vector $\hat{\mathbf{F}}(k)$ denotes the space Fourier transform of $\mathbf{F}(z)$: $\hat{\mathbf{F}}(k) = \int_{-\infty}^{+\infty} \mathbf{F}(z) e^{-ikz} dz$.

As proved in Ref. [26], the solution given by Eqs. (7) and (8) is actually based on the so-called Auld's real biorthogonality relationship [29] and remains applicable for non-propagating modes, fully anisotropic materials and lossy waveguides (in particular, the matrix of material properties $\mathbf{C}$ can be complex to handle viscoelastic materials). The normalization factor in Eq. (8) is given by $Q_{m,-m} = i\frac{\omega}{4}\left(\mathbf{T}_{-m}^{\mathrm{T}}\mathbf{U}_m - \mathbf{U}_{-m}^{\mathrm{T}}\mathbf{T}_m\right)$ and usually differs from the averaged power flow of a mode. In the particular case of propagating modes in lossless waveguides ($k_m \in \mathbb{R}$), the solution can be simplified thanks to the so-called Auld's complex biorthogonality relationship [29] and $Q_{m,-m}$ becomes equal to the modal averaged power flow. The reader may refer to [26] for more details on this topic.

However as shown further, the introduction of rotational symmetry in the waveguide formulation breaks the skew-symmetry of the matrix in Eq. (4) so that Eqs. (7) and (8) are no longer applicable.

3. Formulation with rotational symmetry

Let us denote N the order of the rotational symmetry of the problem. As shown in Fig. 3, the structure is divided into N rotationally periodic cells. In the following, the left superscript s will be used to identify the cell index of elastodynamic fields ($s = 0, 1, ..., N-1$). The vectors ${}^s\mathbf{U}$ and ${}^s\mathbf{F}$ will denote the displacement vector of the cell s and the external force vector applied to the cell s respectively. The cell $s = 0$ will be considered as the reference cell, that is to say, the unique cell that needs to be discretized by finite elements. For conciseness of notations, one will drop out the superscript $s = 0$ for the reference cell: $\mathbf{U} = {}^0\mathbf{U}$, $\mathbf{F} = {}^0\mathbf{F}$.

3.1. Free response

Let us consider the equilibrium equation for the reference cell. This equation is given by Eq. (4). The displacement and force vectors are partitioned as follows:

$$\mathbf{U} = \begin{bmatrix} \mathbf{U}_l \\ \mathbf{U}_i \\ \mathbf{U}_r \end{bmatrix}, \quad \mathbf{F} = \begin{bmatrix} \mathbf{F}_l \\ \mathbf{F}_i \\ \mathbf{F}_r \end{bmatrix} \tag{9}$$

where the subscripts l and r stand for the left and right degrees of freedom (dofs), associated with the left and right boundaries of the rotationally periodic cell of the cross-section – see Fig. 3 (see also Figs. 4 and 9 for examples). The subscript i is left for the remaining dofs (internal dofs).

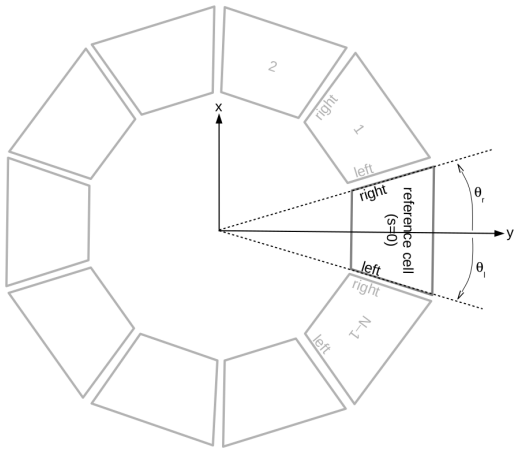

Figure 3: Sketch of a rotationally symmetric cross-section of order N with its reference unit cell. θ_l and θ_r denote the angles of the left and right boundaries of the reference cell respectively.

Since the free response is considered here, there is no external force and the vector $\mathbf{F}$ must be understood as the internal force vector acting on the reference cell ($\mathbf{F} = \mathbf{F}_{\text{int}}$). These internal forces correspond to the forces acting on the left and right boundaries, which are connected to the adjacent cells. Hence, there is no force acting on internal dofs ($\mathbf{F}_i = \mathbf{0}$).

The Bloch-Floquet boundary conditions for a given field ϕ and its dual variable ψ are $\phi_r = \lambda\phi_l$ and $\psi_r = -\lambda\psi_l$ [30, 31], where $\lambda = \mathrm{e}^{\mathrm{i}\mu}$ and $\mathrm{i}\mu$ is called the propagation constant. However, the periodicity to be applied in this paper is of rotational type and concerns a nonscalar field (the displacement vector). The Bloch-Floquet conditions must then be expressed along the circumferential direction in an appropriate frame, namely the cylindrical coordinate system.

Since the displacement components $\mathbf{U}_l$ and $\mathbf{U}_r$ are initially expressed in a (x, y, z) Cartesian frame, they must be transformed to the (r, θ, z) cylindrical frame. Cartesian and cylindrical coordinates are related by $(x, y) = (r\cos\theta, r\sin\theta)$ ($r = 0$ corresponding to the center of rotational symmetry). Let us denote $\mathbf{Q}_l$ and $\mathbf{Q}_r$ the transformation matrices of $\mathbf{U}_l$ and $\mathbf{U}_r$ from the Cartesian to the cylindrical frames. The rotationally periodic conditions for the displacement and force vector fields are then:

$$\mathbf{Q}_r\mathbf{U}_r = \lambda\mathbf{Q}_l\mathbf{U}_l \tag{10a}$$

$$\mathbf{Q}_r\mathbf{F}_r = -\lambda\mathbf{Q}_l\mathbf{F}_l \tag{10b}$$

The transformation matrices $\mathbf{Q}_{l,r}$ are block diagonal and comprise three-by-three sub-matrices $\mathbf{q}_{l,r}$ (for the three components of the displacement vector at every node) defined as:

$$\mathbf{q}_{l,r} = \begin{bmatrix} \cos\theta_{l,r} & \sin\theta_{l,r} & 0 \\ -\sin\theta_{l,r} & \cos\theta_{l,r} & 0 \\ 0 & 0 & 1 \end{bmatrix} \tag{11}$$

where θ_l and θ_r are the angles of the left and right boundaries respectively (see Fig. 3). These sub-matrices are rotation matrices and are hence orthogonal. Therefore, the following properties hold: $\mathbf{Q}_{l,r}^{-1} = \mathbf{Q}_{l,r}^{\mathrm{T}}$.

As depicted by Fig. 3, the wave fields at the right boundary of the last cell ($s = N - 1$) should be equal to the fields at the left boundary of the reference cell ($s = 0$). This leads to the equation $\lambda^N = 1$, or equivalently: $\mu = 2n\pi/N$, where $n = 0, 1, ..., N - 1$. Therefore, λ is a function of the integer n and can be viewed as a fixed user-defined parameter written as follows:

$$\lambda(n) = \mathrm{e}^{\mathrm{i}2n\pi/N} \tag{12}$$

Instead of numbering the circumferetial order n from 0 to $N - 1$, it is convenient to adopt the following numbering:

$$n = \begin{cases} -\frac{N}{2} + 1, ..., 0, ..., \frac{N}{2} & \text{for } N \text{ even} \\ -\frac{N-1}{2}, ..., 0, ..., \frac{N-1}{2} & \text{for } N \text{ odd} \end{cases} \tag{13}$$

Such a numbering will be of particular interest in Sec. 3.2 and enables to pair right-handed modes (rotating anti-clockwise around the z-axis) with left-handed modes (rotating clockwise). Owing to the $\mathrm{e}^{\mathrm{i}(\mu(n)-\omega t)}$ convention used in this paper, right-handed modes are such that $n > 0$ while left-handed modes are such that $n < 0$. The modes $n = 0$ are rotationally symmmetric.

From Eq. (10a) written for a given n, the displacement dofs can be related by:

$$\mathbf{U} = \mathbf{R}(n)\tilde{\mathbf{U}}, \quad \mathbf{R}(n) = \begin{bmatrix} \mathbf{I} & \mathbf{0} \\ \mathbf{0} & \mathbf{I} \\ \lambda(n)\mathbf{Q}_r^{-1}\mathbf{Q}_l & \mathbf{0} \end{bmatrix}, \quad \tilde{\mathbf{U}} = \begin{bmatrix} \mathbf{U}_l \\ \mathbf{U}_i \end{bmatrix}. \tag{14}$$

It is noteworthy that the matrix $\mathbf{R}(n)$ has the following property:

$$\overline{\mathbf{R}(n)} = \mathbf{R}(-n) \tag{15}$$

where the overbar denotes complex conjugate. From this property, the following equality holds: $\mathbf{R}(n)^{\mathrm{H}}\mathbf{K}_2^{\mathrm{T}}\mathbf{R}(n) = \left(\mathbf{R}(-n)^{\mathrm{H}}\mathbf{K}_2\mathbf{R}(-n)\right)^{\mathrm{T}}$. Based on the reduced displacement vector $\tilde{\mathbf{U}}$ and setting a space harmonic dependance $\mathrm{e}^{\mathrm{i}kz}$, Eq. (4) can then be rewritten as:

$$\left\{\tilde{\mathbf{K}}_1(n) - \omega^2\tilde{\mathbf{M}}(n) + \mathrm{i}k\left(\tilde{\mathbf{K}}_2(n) - \tilde{\mathbf{K}}_2(-n)^{\mathrm{T}}\right) + k^2\tilde{\mathbf{K}}_3(n)\right\}\tilde{\mathbf{U}} = \mathbf{R}(n)^{\mathrm{H}}\mathbf{F} \tag{16}$$

where $\tilde{\mathbf{K}}_i(n) = \mathbf{R}(n)^{\mathrm{H}}\mathbf{K}_i\mathbf{R}(n)$ $(i = 1, 2, 3)$, $\tilde{\mathbf{M}}(n) = \mathbf{R}(n)^{\mathrm{H}}\mathbf{M}\mathbf{R}(n)$ (the superscript H denotes complex conjugate transpose).

Accounting for the orthogonality of $\mathbf{Q}_{l,r}$, the expansion of the right hand side of Eq. (16) leads to:

$$\mathbf{R}(n)^{\mathrm{H}}\mathbf{F} = \begin{bmatrix} \mathbf{F}_l + \overline{\lambda(n)}\mathbf{Q}_l^{-1}\mathbf{Q}_r\mathbf{F}_r \\ \mathbf{0} \end{bmatrix} \tag{17}$$

From Eq. (10b), one has: $\mathbf{F}_l + \overline{\lambda(n)}\mathbf{Q}_l^{-1}\mathbf{Q}_r\mathbf{F}_r = (1 - |\lambda(n)|^2)\mathbf{F}_l$. This expression indeed vanishes because $|\lambda(n)| = |\mathrm{e}^{\mathrm{i}2n\pi/N}| = 1$, so that:

$$\mathbf{R}(n)^{\mathrm{H}}\mathbf{F} = \mathbf{0} \tag{18}$$

Therefore, Eq. (16) is a homogeneous equation, corresponding to the eigensystem that accounts both for the continuous translational invariance along the axis (using the waveguide formulation) and for the discrete rotational symmetry of the cross-section (thanks to the application of Bloch-Floquet conditions).

Compared to the eigenvalue problem (4), it can be noticed that the matrix $\left(\tilde{\mathbf{K}}_2(n) - \tilde{\mathbf{K}}_2(-n)^{\mathrm{T}}\right)$ is not skew-symmetric for $n \neq 0$ and $n \neq N/2$ (the particular cases $n = 0$ and $n = N/2$ yield $\lambda = 1$ and $\lambda = -1$ respectively, which preserves the skew-symmetry property of the matrix). Note that left multiplying by the transpose of $\mathbf{R}(n)$, instead of the complex transpose, does not enable to cancel the right hand side of Eq. (16) (the product $\mathbf{R}(n)^{\mathrm{T}}\mathbf{F}$ leads to the factor $(1 - \lambda^2)$, which does not vanish except for $n = 0$ and $n = N/2$. This break of symmetry means that modes computed with the rotationally symmetric formulation for a given circumferential order n do not necessarily occur in pairs of opposite wavenumbers. As a consequence, the forced response calculation as given in Ref. [26] and recalled by Eqs. (7) and (8) is no longer applicable. A specific biorthogonality relation is required as derived in the next subsection.

Throughout this paper, the mth eigensolution obtained for a given circumferential order n will be denoted as follows:

$$\{k_m^{(n)}, \tilde{\mathbf{U}}_m^{(n)}\} \tag{19}$$

Left-multipying both sides of Eq. (6) by $\mathbf{R}(n)^{\mathrm{H}}$, the modal traction associated with the eigendisplacement $\tilde{\mathbf{U}}_m^{(n)}$ is therefore:

$$\tilde{\mathbf{T}}_m^{(n)} = \left(\tilde{\mathbf{K}}_2(-n)^{\mathrm{T}} + ik_m^{(n)}\tilde{\mathbf{K}}_3(n)\right)\tilde{\mathbf{U}}_m^{(n)} \tag{20}$$

where $\tilde{\mathbf{T}}_m^{(n)} = \mathbf{R}(n)^{\mathrm{H}}\mathbf{T}_m^{(n)}$ and $\mathbf{U}_m^{(n)} = \mathbf{R}(n)\tilde{\mathbf{U}}_m^{(n)}$.

3.2. Biorthogonality relationship

The eigenproblem (16) is unsymmetric. Left and right eigenvectors are different from each other. The right eigensolution $\{k_m^{(n)}, \tilde{\mathbf{U}}_m^{(n)}\}$ satisfies:

$$\left\{\tilde{\mathbf{K}}_1(n) - \omega^2\tilde{\mathbf{M}}(n) + \mathrm{i}k_m^{(n)}\left(\tilde{\mathbf{K}}_2(n) - \tilde{\mathbf{K}}_2(-n)^{\mathrm{T}}\right) + k_m^{(n)2}\tilde{\mathbf{K}}_3(n)\right\}\tilde{\mathbf{U}}_m^{(n)} = \mathbf{0} \tag{21}$$

The left eigensolution $\{k_m^{(n)}, \tilde{\mathbf{V}}_m^{(n)}\}$ satisfies:

$$\tilde{\mathbf{V}}_m^{(n)\mathrm{T}}\left\{\tilde{\mathbf{K}}_1(n) - \omega^2\tilde{\mathbf{M}}(n) + \mathrm{i}k_m^{(n)}\left(\tilde{\mathbf{K}}_2(n) - \tilde{\mathbf{K}}_2(-n)^{\mathrm{T}}\right) + k_m^{(n)2}\tilde{\mathbf{K}}_3(n)\right\} = \mathbf{0} \tag{22}$$

Noticing the properties that result from Eq. (15):

$$\tilde{\mathbf{K}}_1^{(n)\mathrm{T}} = \tilde{\mathbf{K}}_1(-n), \quad \tilde{\mathbf{K}}_3^{(n)\mathrm{T}} = \tilde{\mathbf{K}}_3(-n), \quad \tilde{\mathbf{M}}^{(n)\mathrm{T}} = \tilde{\mathbf{M}}(-n) \tag{23}$$

and taking the transpose of Eq. (22), one gets:

$$\left\{\tilde{\mathbf{K}}_1(-n) - \omega^2\tilde{\mathbf{M}}(-n) - \mathrm{i}k_m^{(n)}\left(\tilde{\mathbf{K}}_2(-n) - \tilde{\mathbf{K}}_2(n)^{\mathrm{T}}\right) + k_m^{(n)2}\tilde{\mathbf{K}}_3(-n)\right\}\tilde{\mathbf{V}}_m^{(n)} = \mathbf{0} \tag{24}$$

which shows that $\{-k_m^{(n)}, \tilde{\mathbf{V}}_m^{(n)}\}$ is a right eigensolution for the opposite circumferential order $-n$. For this solution, the following notation will be adopted:

$$\{-k_m^{(n)}, \tilde{\mathbf{V}}_m^{(n)}\} = \{k_{-m}^{(-n)}, \tilde{\mathbf{U}}_{-m}^{(-n)}\} \tag{25}$$

What Eq. (24) means is that if $k_m^{(n)}$ is an eigenvalue for the order n, then $-k_m^{(n)} = k_{-m}^{(-n)}$ is an eigenvalue for the order $-n$. Hence, the eigenproblem has two subsets of eigensolutions, $(k_m^{(n)}, \tilde{\mathbf{U}}_m^{(n)})$ and $(k_{-m}^{(-n)}, \tilde{\mathbf{U}}_{-m}^{(-n)})$ $(m = 1, ..., M)$ representing M pairs of opposite-going modes, travelling in the opposite z-direction and also rotating in the opposite direction.

Equation (22) is rewritten with the notation (25) for a given mode m' and then right-multiplied by the eigenvector $\tilde{\mathbf{U}}_m^{(n)}$:

$$\tilde{\mathbf{U}}_{-m'}^{(-n)\mathrm{T}}\left\{\tilde{\mathbf{K}}_1(n) - \omega^2\tilde{\mathbf{M}}(n) - \mathrm{i}k_{-m'}^{(-n)}\left(\tilde{\mathbf{K}}_2(n) - \tilde{\mathbf{K}}_2(-n)^{\mathrm{T}}\right) + k_{-m'}^{(-n)2}\tilde{\mathbf{K}}_3(n)\right\}\tilde{\mathbf{U}}_m^{(n)} = \mathbf{0} \tag{26}$$

The above equation is then substracted from Eq. (21) left-mutliplied by $\mathbf{U}_{-m'}^{(-n)\mathrm{T}}$, which leads to the following equation:

$$\mathrm{i}\left(k_m^{(n)} + k_{-m'}^{(-n)}\right)\tilde{\mathbf{U}}_{-m'}^{(-n)\mathrm{T}}\left\{\tilde{\mathbf{K}}_2(n) - \tilde{\mathbf{K}}_2(-n)^{\mathrm{T}} - \mathrm{i}\left(k_m^{(n)} - k_{-m'}^{(-n)}\right)\tilde{\mathbf{K}}_3(n)\right\}\tilde{\mathbf{U}}_m^{(n)} = \mathbf{0} \tag{27}$$

Introducing the modal traction expression (20), the above equation can be rewritten as the biorthogonality relationship:

$$\mathrm{i}\frac{\omega}{4}\left(\tilde{\mathbf{T}}_{-m'}^{(-n)\mathrm{T}}\tilde{\mathbf{U}}_m^{(n)} - \tilde{\mathbf{U}}_{-m'}^{(-n)\mathrm{T}}\tilde{\mathbf{T}}_m^{(n)}\right) = Q_{m,-m'}^{(n,-n)}\delta_{mm'} \tag{28}$$

where $\delta_{mm'}$ denotes Kronecker's symbol. This relation can actually be viewed as a discrete version of Auld's real biorthogonality relationship [29], specific to the rotationally symmetric formulation. No specific assumption is needed in the nature of modes and materials so that this relationship remains applicable for non-propagating modes, fully anisotropic materials and lossy waveguides.

3.3. Equilibrium equation for the forced response

Starting from Eq. (4) written for the cell s, the forced response problem of this cell is given by the following equation:

$$(\mathbf{K}_1 - \omega^2\mathbf{M})^s\mathbf{U} + (\mathbf{K}_2 - \mathbf{K}_2^{\mathrm{T}})^s\mathbf{U}_{,z} - \mathbf{K}_3{}^s\mathbf{U}_{,zz} = {}^s\mathbf{F} = {}^s\mathbf{F}_{\mathrm{ext}} + {}^s\mathbf{F}_{\mathrm{int}} \tag{29}$$

where the force vector has been split into external forces and internal forces. Note that the matrices on the left-hand side are independent on s because the geometry is rotationally symmetric, which implies that the displacement and force components in ${}^s\mathbf{U}$ and ${}^s\mathbf{F}$ must be understood as written in a local frame rotated by an angle $2\pi s/N$ with respect to the frame of the reference cell.

The following circumferential order decomposition is adopted (see Appendix A):

$$ {}^{s}\mathbf{U} = \sum_{n} \mathbf{U}^{(n)} \mathrm{e}^{\mathrm{i}2\pi ns/N}, \quad {}^{s}\mathbf{F}_{\mathrm{ext}} = \sum_{n} \mathbf{F}_{\mathrm{ext}}^{(n)} \mathrm{e}^{\mathrm{i}2\pi ns/N}, \quad {}^{s}\mathbf{F}_{\mathrm{int}} = \sum_{n} \mathbf{F}_{\mathrm{int}}^{(n)} \mathrm{e}^{\mathrm{i}2\pi ns/N}, \tag{30} $$

where it is recalled that the left superscripts for the reference cell have been dropped out ($\mathbf{U}^{(n)} = {}^{0}\mathbf{U}^{(n)}$, $\mathbf{F}_{\mathrm{ext}}^{(n)} = {}^{0}\mathbf{F}_{\mathrm{ext}}^{(n)}$ and $\mathbf{F}_{\mathrm{int}}^{(n)} = {}^{0}\mathbf{F}_{\mathrm{int}}^{(n)}$). In the above expansions, the nth coefficient is actually uniquely determined thanks to the formula (A.5).

Let us multiply Eq. (29) by the factor $\mathrm{e}^{-\mathrm{i}2\pi n's/N}$ and sum the equation for every cell s:

$$ \left\{ \mathbf{K}_1 - \omega^2 \mathbf{M} + (\mathbf{K}_2 - \mathbf{K}_2^{\mathrm{T}}) \frac{\partial}{\partial z} - \mathbf{K}_3 \frac{\partial^2}{\partial z^2} \right\} \left(\frac{1}{N} \sum_{s=0}^{N-1} {}^{s}\mathbf{U} \mathrm{e}^{-\mathrm{i}2\pi n's/N} \right) = \frac{1}{N} \sum_{s=0}^{N-1} ({}^{s}\mathbf{F}_{\mathrm{ext}} + {}^{s}\mathbf{F}_{\mathrm{int}}) \mathrm{e}^{-\mathrm{i}2\pi n's/N} \tag{31} $$

Using Eq. (30) into (31) together with the formula (A.2), one gets an equilibrium equation written on the reference cell only:

$$ (\mathbf{K}_1 - \omega^2 \mathbf{M}) \mathbf{U}^{(n)} + (\mathbf{K}_2 - \mathbf{K}_2^{\mathrm{T}}) \mathbf{U}_{,z}^{(n)} - \mathbf{K}_3 \mathbf{U}_{,zz}^{(n)} = \mathbf{F}_{\mathrm{ext}}^{(n)} + \mathbf{F}_{\mathrm{int}}^{(n)} \tag{32} $$

The vectors $\mathbf{U}^{(n)}$ and $\mathbf{F}_{\mathrm{int}}^{(n)}$ obey the Bloch-Floquet conditions (10). Hence, following the same steps as in Sec. 3.1, the application of these periodicity conditions to Eq. (32) leads to:

$$ \left(\tilde{\mathbf{K}}_1(n) - \omega^2 \tilde{\mathbf{M}}(n) \right) \tilde{\mathbf{U}}^{(n)} + \left(\tilde{\mathbf{K}}_2(n) - \tilde{\mathbf{K}}_2(-n)^{\mathrm{T}} \right) \tilde{\mathbf{U}}_{,z}^{(n)} - \tilde{\mathbf{K}}_3(n) \tilde{\mathbf{U}}_{,zz}^{(n)} = \tilde{\mathbf{F}}_{\mathrm{ext}}^{(n)} \tag{33} $$

where:

$$ \tilde{\mathbf{F}}_{\mathrm{ext}}^{(n)} = \mathbf{R}(n)^{\mathrm{H}} \, \mathbf{F}_{\mathrm{ext}}^{(n)} \tag{34} $$

Equation (33) is the forced response problem accounting for rotational symmetry. The equation has to be solved for each circumferential order n. The decomposition for ${}^{s}\mathbf{U}$ in Eq. (30) shows that the response in an arbitrary cell s can be obtained once the response for the reference cell $\mathbf{U}^{(n)}$ has been solved for each n.

As shown by Eq. (A.5), the coefficients $\mathbf{F}_{\mathrm{ext}}^{(n)}$ can be determined from the applied external forces ${}^{s}\mathbf{F}_{\mathrm{ext}}$ ($s = 0, ..., N-1$) as follows:

$$ \mathbf{F}_{\mathrm{ext}}^{(n)} = \frac{1}{N} \sum_{s=0}^{N-1} {}^{s}\mathbf{F}_{\mathrm{ext}} \mathrm{e}^{-\mathrm{i}2\pi ns/N} \tag{35} $$

For clarity, let us consider two excitation examples. First, if the excitation is rotationally symmetric (${}^{s}\mathbf{F}_{\mathrm{ext}} = {}^{0}\mathbf{F}_{\mathrm{ext}} = \mathbf{F}_{\mathrm{ext}}$ for any s), then Eq. (35) yields:

$$ \mathbf{F}_{\mathrm{ext}}^{(n)} = \frac{1}{N} \mathbf{F}_{\mathrm{ext}} \sum_{s=0}^{N-1} \mathrm{e}^{-\mathrm{i}2\pi ns/N} = \begin{cases} \mathbf{F}_{\mathrm{ext}} & \text{for } n = 0 \\ 0 & \text{for } n \neq 0 \end{cases} \tag{36} $$

Second, if the excitation is localized on a single cell (the reference cell $s = 0$ for convenience), then Eq. (35) yields:

$$ \mathbf{F}_{\mathrm{ext}}^{(n)} = \frac{1}{N} \mathbf{F}_{\mathrm{ext}} \quad \text{for any } n \tag{37} $$

3.4. Solution of the forced response

The solution to Eq. (33) is expanded on the eigenmodes:

$$ \tilde{\mathbf{U}}^{(n)}(z) = \sum_{m} \alpha_m^{(n)}(z) \tilde{\mathbf{U}}_m^{(n)} \tag{38} $$

where the $\alpha_m^{(n)}(z)$ are the modal coefficients to be determined. As done analytically in Refs. [29, 32], an elegant way of determining the forced response is to start from a reciprocity relationship.

Let us consider two states A and B, with displacements denoted as $\tilde{\mathbf{U}}_A^{(n)}$ and $\tilde{\mathbf{U}}_B^{(-n)}$, satisfying Eq. (33) for the circumferential order n with an external force $\tilde{\mathbf{F}}_A^{(n)}$ and for the order $-n$ with a force $\tilde{\mathbf{F}}_B^{(-n)}$ respectively. One can write:

$$\tilde{\mathbf{U}}_B^{(-n)\mathrm{T}}\left\{\left(\tilde{\mathbf{K}}_1(n)-\omega^2\tilde{\mathbf{M}}(n)\right)\tilde{\mathbf{U}}_A^{(n)}+\left(\tilde{\mathbf{K}}_2(n)-\tilde{\mathbf{K}}_2(-n)^{\mathrm{T}}\right)\tilde{\mathbf{U}}_{A,z}^{(n)}-\tilde{\mathbf{K}}_3(n)\tilde{\mathbf{U}}_{A,zz}^{(n)}\right\}=\tilde{\mathbf{U}}_B^{(-n)\mathrm{T}}\tilde{\mathbf{F}}_A^{(n)}, \tag{39a}$$

$$\tilde{\mathbf{U}}_A^{(n)\mathrm{T}}\left\{\left(\tilde{\mathbf{K}}_1(-n)-\omega^2\tilde{\mathbf{M}}(-n)\right)\tilde{\mathbf{U}}_B^{(-n)}+\left(\tilde{\mathbf{K}}_2(-n)-\tilde{\mathbf{K}}_2(n)^{\mathrm{T}}\right)\tilde{\mathbf{U}}_{B,z}^{(-n)}-\tilde{\mathbf{K}}_3(-n)\tilde{\mathbf{U}}_{B,zz}^{(-n)}\right\}=\tilde{\mathbf{U}}_A^{(n)\mathrm{T}}\tilde{\mathbf{F}}_B^{(-n)} \tag{39b}$$

Taking the transpose of (39b) and substracting it from Eq. (39a) yields thanks to the properties (23):

$$\frac{\partial}{\partial z}\left\{\tilde{\mathbf{U}}_B^{(-n)\mathrm{T}}\left(\tilde{\mathbf{K}}_2(n)-\tilde{\mathbf{K}}_2(-n)^{\mathrm{T}}\right)\tilde{\mathbf{U}}_A^{(n)}-\tilde{\mathbf{U}}_B^{(-n)\mathrm{T}}\tilde{\mathbf{K}}_3(n)\tilde{\mathbf{U}}_{A,z}^{(n)}+\tilde{\mathbf{U}}_{B,z}^{(-n)\mathrm{T}}\tilde{\mathbf{K}}_3(n)\tilde{\mathbf{U}}_A^{(n)}\right\}=\tilde{\mathbf{U}}_B^{(-n)\mathrm{T}}\tilde{\mathbf{F}}_A^{(n)}-\tilde{\mathbf{U}}_A^{(n)\mathrm{T}}\tilde{\mathbf{F}}_B^{(-n)} \tag{40}$$

Introducing the traction vector as defined from Eq. (6), the above equation can be rewritten as:

$$\frac{\partial}{\partial z}\left\{\tilde{\mathbf{T}}_B^{(-n)\mathrm{T}}\tilde{\mathbf{U}}_A^{(n)}-\tilde{\mathbf{U}}_B^{(-n)\mathrm{T}}\tilde{\mathbf{T}}_A^{(n)}\right\}=\tilde{\mathbf{U}}_B^{(-n)\mathrm{T}}\tilde{\mathbf{F}}_A^{(n)}-\tilde{\mathbf{U}}_A^{(n)\mathrm{T}}\tilde{\mathbf{F}}_B^{(-n)} \tag{41}$$

Note that this identity can be interpreted as a discrete version of Auld's real reciprocity relation [29]. In order to obtain the modal coefficients $\alpha_m^{(n)}(z)$, state A is chosen as the forced response we are looking for and state B is set to the virtual propagation state of a single mode $-m'$. Therefore, we set:

$$\tilde{\mathbf{U}}_A^{(n)}=\sum_m \alpha_m^{(n)}(z)\tilde{\mathbf{U}}_m^{(n)},\quad \tilde{\mathbf{T}}_A^{(n)}=\sum_m \alpha_m^{(n)}(z)\tilde{\mathbf{T}}_m^{(n)},\quad \tilde{\mathbf{F}}_A^{(n)}=\tilde{\mathbf{F}}_{\mathrm{ext}}^{(n)}(z), \tag{42a}$$

$$\tilde{\mathbf{U}}_B^{(-n)}=\tilde{\mathbf{U}}_{-m'}^{(-n)}\exp\left(\mathrm{i}k_{-m'}^{(-n)}z\right),\quad \tilde{\mathbf{T}}_B^{(-n)}=\tilde{\mathbf{T}}_{-m'}^{(-n)}\exp\left(\mathrm{i}k_{-m'}^{(-n)}z\right),\quad \tilde{\mathbf{F}}_B^{(-n)}=\mathbf{0} \tag{42b}$$

Using Eq. (42b) into Eq. (41) and exploiting the biorthogonality relationship (28), the summation on the left-hand side has only a single nonzero term, yielding an uncoupled ordinary differential equation for each $\alpha_m^{(n)}(z)$:

$$\frac{\mathrm{d}}{\mathrm{d}z}\left\{\alpha_m^{(n)}(z)\exp\left(-\mathrm{i}k_m^{(n)}z\right)\right\}=\frac{\mathrm{i}\omega}{4Q_{m,-m}^{(n,-n)}}\tilde{\mathbf{U}}_{-m}^{(-n)\mathrm{T}}\tilde{\mathbf{F}}_{\mathrm{ext}}^{(n)}(z)\exp\left(-\mathrm{i}k_m^{(n)}z\right) \tag{43}$$

Solving this equation for waves travelling toward the positive z-direction and z outside the source region (one assumes that the excitation is zero outside a finite interval along z) finally leads to the forced solution:

$$\tilde{\mathbf{U}}^{(n)}=\sum_{m>0}\mathbf{E}_m^{(n)}\hat{\tilde{\mathbf{F}}}_{\mathrm{ext}}^{(n)}(k_m^{(n)})\mathrm{e}^{\mathrm{i}k_m^{(n)}z} \tag{44}$$

where $\mathbf{E}_m^{(n)}$ is the excitability matrix defined by:

$$\mathbf{E}_m^{(n)}=\frac{\mathrm{i}\omega}{4Q_{m,-m}^{(n,-n)}}\tilde{\mathbf{U}}_m^{(n)}\tilde{\mathbf{U}}_{-m}^{(-n)\mathrm{T}} \tag{45}$$

Note that the summation in Eq. (44) is performed on positive-going waves only (denoted by positive values of m). The solution outside the source region for waves travelling toward the negative z-direction is identical to Eq. (44) but with a minus sign and a summation on negative-going modes ($m<0$). The vector $\hat{\tilde{\mathbf{F}}}_{\mathrm{ext}}^{(n)}(k)$ is defined as the space Fourier transform of $\tilde{\mathbf{F}}_{\mathrm{ext}}^{(n)}(z)$: $\hat{\tilde{\mathbf{F}}}_{\mathrm{ext}}^{(n)}(k)=\int_{-\infty}^{+\infty}\tilde{\mathbf{F}}_{\mathrm{ext}}^{(n)}(z)\mathrm{e}^{-\mathrm{i}kz}\mathrm{d}z$. In the excitability matrix, the term $\left(\mathbf{E}_m^{(n)}\right)_{ij}$ represents the displacement amplitude for the order n of the single wavemode m at dof i when a unit force acts at dof j.

Compared to Eqs. (7) and (8), the solution given by Eqs. (44) and (45) requires two computations, one for the circumferential order $+n$ and another one for the opposite order $-n$. However, note that solving the left eigenproblem (22) is not needed.

Finally, the response in any cell s can be recovered thanks to Eq. (30), which gives:

$${}^{s}\tilde{\mathbf{U}}=\sum_n\sum_{m>0}\mathbf{E}_m^{(n)}\tilde{\mathbf{F}}_{\mathrm{ext}}^{(n)}(k_m^{(n)})\mathrm{e}^{\mathrm{i}k_m^{(n)}z}\mathrm{e}^{\mathrm{i}2\pi ns/N} \tag{46}$$

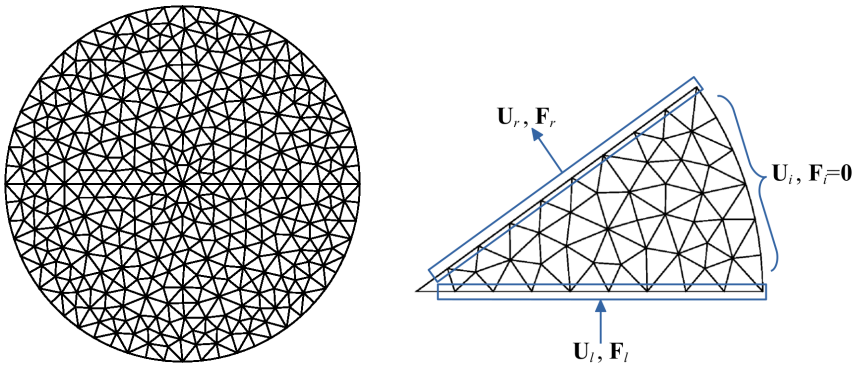

Figure 4: FE mesh of the cross-section of a cylindrical waveguide: (a) complete model (4743 dofs), (b) reduced model of a rotationally symmetric cell with $N = 10$ (531 dofs).

and the solution in the space-time domain (z, t) is obtained from the inverse time Fourier transform of ${}^s\tilde{\mathbf{U}}$, given by $\frac{1}{2\pi}\int_{-\infty}^{+\infty} {}^s\tilde{\mathbf{U}} \mathrm{e}^{-\mathrm{i}\omega t}\mathrm{d}\omega$.

As a side remark, the traveling direction in elastic waveguides of a given mode has to be determined from the sign of energy velocity for purely propagating modes ($k_m^{(n)} \in \mathbb{R}$) and from the sign of $\mathrm{Im}\, k_m^{(n)}$ otherwise. The real part of wavenumbers cannot be used because backward modes may occur (the energy and phase velocities of such modes have opposite signs).

4. The cylindrical test case

In this section, the method is validated for a cylindrical waveguide by comparing results with those obtained from the waveguide formulation of a complete cross-section (*i.e.* formulation recalled in Sec. 2). Both the free response and the forced response are computed.

Assuming an isotropic material, results for the free response are given as dispersion curves for the normalized energy velocity v_e/c_s as a function of the normalized frequency $\omega a/c_s$, where $c_s = \sqrt{E/2\rho(1+\nu)}$ denotes the shear wave velocity and a is the radius of the cylinder (E, ρ and ν denote Young's modulus, mass density and Poisson's ratio respectively). The energy velocity v_e of a given mode $\mathbf{U}_m^{(n)}$ can be post-processed as follows (see Ref. [33] for instance):

$$v_e = \frac{2\omega \mathrm{Im}\left\{\mathbf{U}_m^{(n)\mathrm{H}}(\mathbf{K}_2^{\mathrm{T}} + ik\mathbf{K}_3)\mathbf{U}_m^{(n)}\right\}}{\mathrm{Re}\left\{\mathbf{U}_m^{(n)\mathrm{H}}(\mathbf{K}_1 + \omega^2\mathbf{M} + ik(\mathbf{K}_2 - \mathbf{K}_2^{\mathrm{T}}) + k^2\mathbf{K}_3)\mathbf{U}_m^{(n)}\right\}} \tag{47}$$

where $\mathbf{U}_m^{(n)} = \mathbf{R}(n)\tilde{\mathbf{U}}_m^{(n)}$. The Poisson coefficient of the isotropic material is set to $\nu = 0.28$.

The FE discretization of the rotationally periodic cell is generated so that left and right boundaries have a compatible mesh that allows a direct connection between left and right nodes. Six-node triangles are used (*i.e.* quadratic interpolating functions). The FE meshes of this paper have been built from the free software Gmsh [34]. Figure 4 shows the FE meshes used for the discretization of the complete cross-section and for the unit cell. Owing to the circular cross-section, the angular sector of the unit cell can be arbitrarily thin. In this example, N is set to 10 (the rotationally symmetric model is hence reduced to a sector of angle $2\pi/10$). The full cross-section mesh has been built from the reduced one in order to get rid of the FE discretization error between both models. The finite elements are six-node triangles whose length l_e satisfies the following meshing criterion: $l_e < \lambda/5$, where $\lambda = 2\pi c_s/\omega_{\max}$ is the smallest wavelength of the problem. Note that the node located at the center of rotational symmetry ($r = 0$) constitutes a special case: Bloch-Floquet conditions are not applied at this point. Instead, a zero displacement has to be enforced in the transverse directions if $n = 0$ or in the axial direction otherwise.

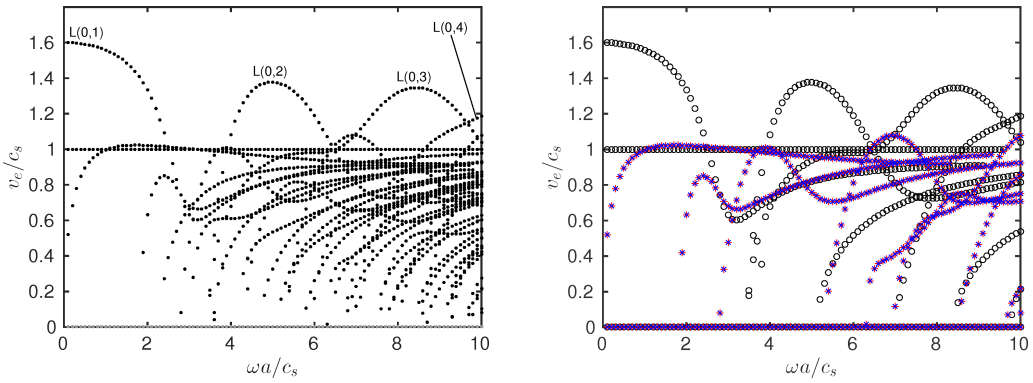

Figure 5: Energy velocity dispersion curves in a cylindrical waveguide computed with: (a) the complete model, (b) the reduced model for $n = 0$ (∘), $n = +1$ (red +) and $n = -1$ (blue ×). Color online.

4.1. Free response

Figure 5 plots the normalized energy velocity dispersion curves computed with the complete model and with the reduced model for $n = 0$ and $n = \pm 1$. Both models give identical results. For $n = 0$, the reduced model gives axisymmetric propagation modes, which can be of the torsional or compressional type in a cylinder. The modes $n \neq 0$, not axisymmetric, are of the flexural type. Compressional modes have been labeled as L(0,p) in the figure. The missing dispersion curves in Fig. 5b correspond to modes of circumferential order $|n| > 1$, which have been omitted for the clarity of the figure (although not shown, it has been checked that these higher order modes also coincide with those computed with the complete model).

In this example, taking into account the rotational symmetry of the problem has allowed reducing the number of dofs by a factor approximately equal to 10 (531 dofs against 4743) as well as reducing the number of modes to compute by roughly the same factor (30 modes per frequency step for a given n against 300 modes with the complete model). The computation time for a given order n of the reduced model has been found about 80 times faster than with the complete model.

4.2. Forced response

Let us consider a point force excitation located at the center of the circular cross-section ($x = y = z = 0$) with a unit amplitude (F=1 Newton). Two orientation cases are considered.

The first case corresponds to an orientation of the point force in the z-direction (waveguide axis) so that the excitation is rotationally symmetric (Eq. (36) applies) and only the L(0,p) modes are excited. Figure 6 plots the modulus of modal excitability $e = (\mathbf{E}_m^{(0)})_{ii}$ post-processed at the center and in the z-direction with the reduced model (the index i here corresponds to the z-displacement degree of freedom of the center node). Figure 6 also plots the excitability calculated from Eq. (8) with the complete model. As expected, the results obtained with both models agree since Eq. (45) degenerates to Eq. (8) for the particular case $n = 0$ (in this particular case, the skew-symmetry property is not broken by the rotationally symmetric formulation). A curve is missing in the results of the reduced model, which is merely due to the limited number of modes (set to 30 modes per frequency, as previously mentioned) – see upper curve in Fig. 6a (this curve yet corresponds to a non-propagating mode and is of less interest). As can be observed, the excitabilities of L(0,1) and L(0,3) modes near their respective maximum of energy velocity are significantly greater than the excitabilities of L(0,2) and L(0,4) modes. This phenomenon is explained by their mode shapes (not shown for paper conciseness), greater at center for L(0,1) and L(0,3) modes.

The second orientation case corresponds to a point force in the x-direction (perpendicular to the waveguide axis). In this case, the excitation is no longer rotationally symmetric and can be considered as localized in the reference cell (Eq. (37) now applies). As opposed to the previous example, a direct comparison of individual modal excitabilities is difficult for non-axisymmetric modes (*i.e.* flexural modes) because, in the complete model, these modes occur in pairs of equal eigenvalues so that their mode shapes are combined by the eigensolver in an arbitrary way. Instead, one

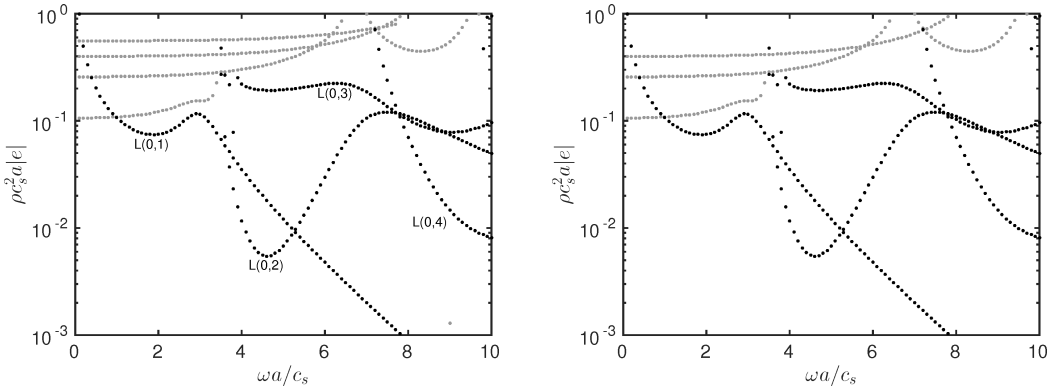

Figure 6: Excitability dispersion curves in a cylindrical waveguide excited by a centered point force oriented in the z-direction, computed with: (a) the complete model (Eq. (8)), (b) the reduced model for $n = 0$ (Eq. (45)). Gray color is used to identify non-propagating modes (Im $k_z \neq 0$).

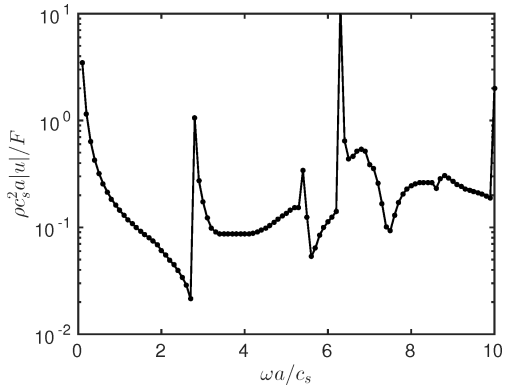

Figure 7: Response at $z = 5a$ in a cylindrical waveguide excited by a centered point force oriented in the x-direction, computed by Eq. (7) for the complete model (•) and by Eq. (44) for the reduced model (continuous line). In the reduced model, only the contribution of modes $n = \pm 1$ has been retained.

compares an example of response calculated at center in the x-direction and at the distance $z = 5a$ from the source. Figure 7 plots the normalized response calculated with the complete model (Eq. (7)) and with the reduced model (Eq. (44)). In the latter case, it has been decided to retain only the contribution of modes $n = \pm 1$ in the response. Despite this, a very good agreement can be observed between both models (the modes $n \neq \pm 1$ have hence a negligible contribution in this example), which validates the forced response calculation proposed in this paper.

4.3. Remarks about anisotropy

It can be noticed in Fig. 5 that the energy velocity curves obtained for the left-handed modes are equal to the right-handed ones (compare $n = +1$ vs. $n = -1$). This property is due to the isotropy of the material. In this case, the eigenvalue spectrum computed for the order $-n$ is identical to the order $+n$, as illustrated in Fig. 8a for $n = \pm 1$ at $\omega a/c_s = 6$.

Let us now consider a particular case of transversely isotropic material, made of unidirectional fiber composite lamina where all fibers are parallel to the z-axis, and such that the matrix of material properties is of the following

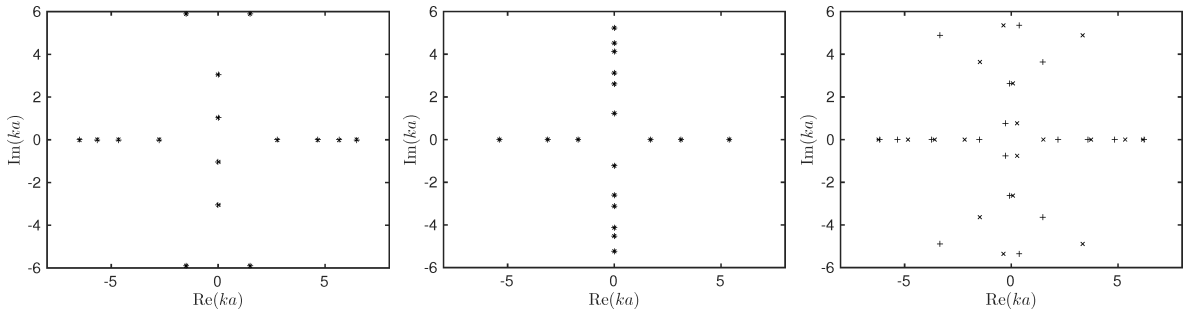

Figure 8: Spectrum computed at $\omega a/c_s = 6$ for $n = +1$ (+) and $n = -1$ (×) in case of: (a) isotropy, (b) transverse isotropy with $\theta = 0°$, (c) transverse isotropy with $\theta = 25°$.

form:

$$\mathbf{C} = \begin{bmatrix} C_{11} & C_{12} & C_{12} & 0 & 0 & 0 \\ C_{12} & C_{11} & C_{12} & 0 & 0 & 0 \\ C_{12} & C_{12} & C_{33} & 0 & 0 & 0 \\ 0 & 0 & 0 & C_{66} & 0 & 0 \\ 0 & 0 & 0 & 0 & C_{66} & 0 \\ 0 & 0 & 0 & 0 & 0 & C_{66} \end{bmatrix} \quad \text{with:} \begin{cases} C_{11} = \frac{(1-\nu)E}{(1+\nu)(1-2\nu)} \\ C_{12} = \frac{\nu E}{(1+\nu)(1-2\nu)} \\ C_{66} = \frac{E}{2(1+\nu)} \end{cases} \tag{48}$$

Although this example is somehow artificial, the material is transversely isotropic if $C_{33} \neq C_{11}$ (and fully isotropic otherwise). We set $C_{33} = 2C_{11}$. As shown in Fig. 8b, the eigenvalues still occur in opposite pairs.

Now, the axis of fibers are rotated by an angle $\theta = 25°$ around the x-axis. The matrix of material properties becomes:

$$\mathbf{C}' = \mathbf{G}(\theta)^{\mathrm{T}} \mathbf{C} \mathbf{G}(\theta) \tag{49}$$

where $\mathbf{G}(\theta)$ is the transformation matrix corresponding to a rotation θ around the x-axis:

$$\mathbf{G}(\theta) = \begin{bmatrix} 1 & 0 & 0 & 0 & 0 & 0 \\ 0 & c^2 & s^2 & 0 & 0 & cs \\ 0 & s^2 & c^2 & 0 & 0 & -cs \\ 0 & 0 & 0 & c & s & 0 \\ 0 & 0 & 0 & -s & c & 0 \\ 0 & -2cs & 2cs & 0 & 0 & c^2 - s^2 \end{bmatrix} \tag{50}$$

with $c = \cos\theta$ and $s = \sin\theta$. As shown in Fig. 8c, the left-handed wavenumbers are no longer equal to the right-handed ones. This means that the modes propagating in a given z-direction behave differently depending on whether they are right- or left-handed. This loss of symmetry is due to the fact that the direction of rotation of modes is sensitive to the inclination of fibers. Yet for all cases (Figs. 8a-c), note that each wavenumber $k_m^{(n)}$ has always an opposite value $k_{-m}^{(-n)} = -k_m^{(n)}$, in agreement with the property shown by Eq. (25).

In the isotropic case (Fig. 8a) and in the transversely isotropic $\theta = 0°$ case (Fig. 8b), one can observe that the eigenvalues for a given order n appear in opposite pairs, $k_m^{(n)}$ and $-k_m^{(n)}$. This suggests that the excitability (45) could be simplified by using an explicit relation between these pairs (see for instance [35]), leading to a degeneracy of the general biorthogonality (28) to a Frazer type biorthogonality [36, 37]. The latter is yet of less interest in this paper because it cannot be applied to the example considered in the next section, involving a form of anisotropy that breaks the symmetry of the spectrum (similarly to Fig. 8c).

5. Application to a multi-wire structure

In this section, the method is applied to a more complex structure by considering a seven-wire strand as shown in Fig. 2. The number of peripheral wires of the strand yields a rotational symmetry of order 6. The material is isotropic

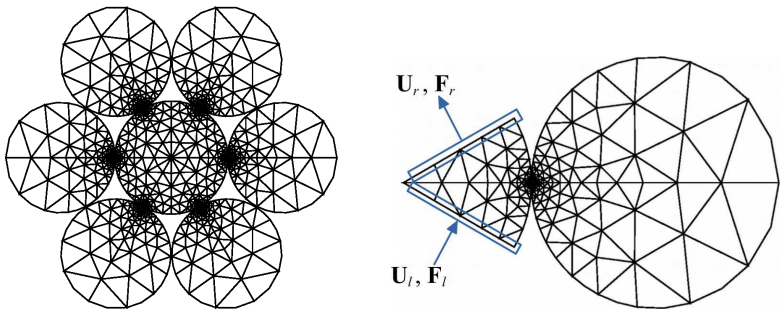

Figure 9: FE mesh of the cross-section of a seven-wire strand: (a) complete model (12369 dofs), (b) reduced model with $N = 6$ of a rotationally symmetric cell (2094 dofs).

($\nu = 0.28$). The characteristic length a is chosen as the radius of the central wire. Because peripheral wires are not straight but helical, the analysis of guided waves requires a specific curvilinear coordinate system, called twisting coordinate system. A twisting system is a particular case of helical system, with zero curvature and a torsion $\tau = 2\pi/L$ (with L denoting the helix pitch of peripheral wires). In this twisting system, the cross-section of the whole structure remains continuously translationally invariant so that guided waves truly exist [33]. The elastodynamic operators must be rewritten in the twisting coordinate system yielding expressions for $\mathbf{L}_{xy}$ and $\mathbf{L}_z$ that are different from Eq. (1) and depend on τ. Furthermore, the strand is prestressed with a 0.6% elongation, which further modifies the operators.

The reader may refer to [38, 39, 18] for details about the modeling of prestressed seven-wire strands. Although more involved than that described in Sec. 2, the formulation leads to an eigensystem which keeps the same form as Eq. (4). Therefore, the whole procedure described in Sec. 3 remains applicable. Similarly to the previous section, results obtained with the proposed method are compared with those obtained with a complete model, which has been thoroughly studied in Refs. [18, 40]. Figure 9 shows the FE meshes used for the discretization of the complete cross-section and for the unit cell. As in Sec. 4, the full cross-section mesh has been built from the reduced one in order to get rid of the FE discretization error. The finite elements are six-node triangles obeying the same meshing criterion as before ($l_e < \lambda/5$), but the meshes are refined near interwire regions in order to accurately account for contact phenomena [18]. In this paper, the radius of peripheral wires is set to $0.967a$ and $\tau a = 0.0705$.

It is noteworthy that the diameter of peripheral wires (smaller than the central wire) is such that they do not contact each other. This is a widespread design criterion to minimize friction effects [41]. The gap between peripheral wires is indeed small and not visible in Fig. 9a. It remains nonzero in the prestressed case also [39]. Since no contact occurs between peripheral wires, Bloch-Floquet conditions are only applied in the central wire (as depicted in Fig. 9b). Hence, contact occurs only between the central wire and the peripheral ones. Infinite friction is assumed in the model (i.e. perfectly stick contact conditions). As thoroughly discussed in Ref. [40], this assumption has shown to give satisfying agreement with available experimental results (further experimental works are out-of-the-scope of the present paper).

5.1. Free response

Figure 10 plots the normalized energy velocity dispersion curves obtained with the complete model and the reduced model for $n = 0$ and $n = \pm 1$. Results coincide with each other (modes calculated for $n = \pm 2, 3$ are not shown for conciseness). As can be observed, seven-wire strands are complex structures involving many dispersion curves owing to the interwire coupling. By analogy with a cylinder, modes can be classified into three categories: longitudinal, torsional and flexural (labeled as L(0,1), T(0,1) and F(1,1) respectively). A detailed description of these curves is out of the scope of this paper but can be found in Ref. [40]. It is yet noteworthy that the modal energy velocities computed for $n = -1$ are different from the order $n = +1$ even though the material is isotropic. Indeed, left-handed ($-n$) and right-handed modes ($+n$) behave differently due to the twist of the structure, which induces an anisotropy of geometric kind. This can be intuitively understood from the three-dimensional rotationally symmetric cell given by Fig. 2b: the twist, right-handed in this example, makes right-handed and left-handed modes have different wave

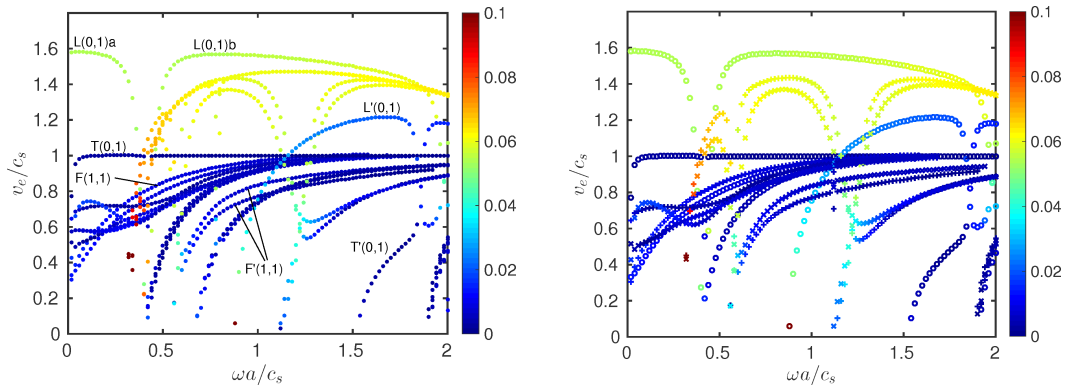

Figure 10: Energy velocity dispersion curves in a seven-wire strand computed with: (a) the complete model, (b) the reduced model for $n = 0$ ($\circ$), $n = +1$ ($+$) and $n = -1$ ($\times$). Colors represent the modal amplitude $|\alpha|$ for an excitation localized inside a peripheral wire. For comparison with the complete model, the coefficient α calculated by the reduced model has been multiplied by $\sqrt{N}$ (color online).

speeds. In Fig. 10b for $n \neq 0$, the fastest modes are right-handed, that is to say co-rotating with the twist (these modes are of longitudinal type, as identified later in Fig. 12).

In this example, the rotationally symmetric formulation has allowed reducing the number of dofs by a factor 6 as well as the number of computed modes by roughly the same factor (20 modes per frequency step against 120 with the complete model). The computation time for a given order n of the reduced model has been found about 10 times faster than with the complete model.

Another advantage of the formulation is the intrinsic classification of modes in terms of their circumferential order n, which can help the analysis of the dynamic behavior of complex structures. This observation coincides with the findings of Refs. [42, 19] dealing with different periodic structures, for which dispersion curves turn out to be much easier to interpret when a reduced unit cell is used.

5.2. *Forced response*

As done in Ref. [40], one considers an excitation localized inside the central wire. Peripheral wires are not excited. The excitation is oriented along the z-direction in order to mainly excite compressional-like mode. The excitation is therefore rotationally symmetric and Eq. (36) applies. The excitation profile is distributed over the cross-section of the central wire as a radial cosine function vanishing at its boundary. One assumes that the excitation is constant with frequency and concentrated at $z = 0$ (the z-dependence of the excitation is the Dirac function so that the space Fourier transform of the excitation does not depend on k).

Figure 11 plots the modal coefficient modulus $|\alpha|$ computed both with the complete model and the reduced one. The modal coefficient α of the reduced model is defined as associated with the normalized displacement mode shapes $\tilde{\mathbf{U}}_m^{(n)} / \sqrt{Q_{m,-m}^{(n,-n)}}$ and is hence defined from Eq. (44) by:

$$\alpha = \frac{\sqrt{\rho a^2 c_s}}{F} \frac{\mathrm{i}\omega}{4\sqrt{Q_{m,-m}^{(n,-n)}}} \tilde{\mathbf{U}}_{-m}^{(-n)\mathrm{T}} \hat{\mathbf{F}}_{\mathrm{ext}}^{(n)}(k_m^{(n)}) \tag{51}$$

where the factor $\sqrt{\rho a^2 c_s}/F$ has been introduced to provide dimensionless results (F denotes the amplitude in Newton of the cosine distribution of the force). Similarly, the modal coefficient α of the complete model is given by the same equation but without the superscripts related to the circumferential orders. The normalized mode shapes of the complete model are given by $\mathbf{U}_m / \sqrt{Q_{m,-m}}$ but it has to be noticed that $Q_{m,-m} = N Q_{m,-m}^{(n,-n)}$. Therefore, the modal coefficient of the reduced model has been multiplied by $\sqrt{N}$ for a direct comparison with the complete one.

As seen in Fig. 11, very good agreement is achieved between both models. From a physical point of view, one can observe that the amplitude of the L'(0,1) mode after its cut-on is greater than the other modes. As explained in

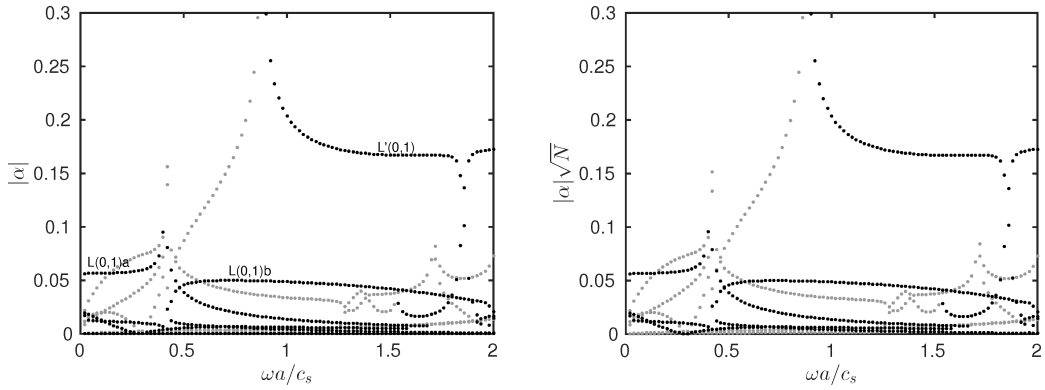

Figure 11: Modulus of modal coefficients $|\alpha|$ as a function of the normalized frequency for a seven-wire strand excited by a longitudinal force localized inside the central wire, computed with: (a) the complete model, (b) the reduced model for $n = 0$. Gray color is used to identify non-propagating modes (Im $k_z \neq 0$).

Ref. [40], this mode could be of interest for nondestructive applications because it is localized inside the central wire as opposed to the global motion of the compressional-like L(0,1)a,b modes.

Let us now consider the same excitation as before but now localized inside a single peripheral wire. Equation (37) now applies. Because the modal behaviour of the structure for a peripheral excitation is more complex than for a central excitation [40], a convenient and compact way of showing the contribution of individual modes to the response is to plot color dispersion curves indicating modal amplitudes $|\alpha|$ – see Fig. 10. Once again, it can be seen that the reduced model is in good agreement with the complete model. Up to a normalized frequency roughly equal to 0.3, the excited mode is mainly the L(0,1)a mode (the motion is of global type). Above this frequency, the motion changes due to the cut-on of several modes (these modes are mainly localized in peripheral wires and combine each other in a complex manner – see Ref. [40] for further details).

5.3. High-frequency results

Although the modal density significantly increases with frequency and complicates the analysis, the rotationally symmetric formulation enables to explore a higher frequency range than the complete model. Figure 12 shows the dispersion curves for $n = 0, \pm 1$ computed with the reduced model up to a normalized frequency $\omega a/c_s = 10$ (100 modes computed per frequency step). Compared to Fig. 9b, the FE mesh has been refined to improve the accuracy of results yielding 18876 dofs. In order to further demonstrate the potentiality of the approach, some material damping has also been included by choosing a frequency independent hysteretic model with longitudinal and shear bulk wave attenuations set to β_l=0.003 and β_s=0.043 Np/wavelength respectively (typical properties for steel, see [43] for instance). The viscoelastic Young's modulus and Poissons ratio are then complex.

The compressional-like modes, labeled 1 to 4 in the figures, still emerge as the fastest modes although these modes suffer from multiple velocity drops due to veering phenomena. A typical example of veering occurs for the 1st low-frequency mode around $\omega a/c_s = 0.4$ (it can be clearly observed in Fig. 10, where the curve splits into two modes labeled L(0,1)a and L(0,1)b). This veering phenomenon has been thoroughly investigated in Ref. [18] and is due to the radial displacement constraint imposed between wires in the contact regions. The results in Fig. 12 suggest that similar veering phenomena may also occur for higher-order longitudinal modes.

Figure 12 also shows the modal coefficient color plots for the same excitation as used for Fig. 10 (excitation localized inside a single peripheral wire and oriented in the axis direction to mainly excite longitudinal modes). Similarly to the cylinder (Fig. 6), the first and third compressional-like modes turn out to be more excitable than the second one. Besides, the modal characteristics as the frequency increases tend to become identical whatever the order n is, which suggests that the coupling between wires tends to decrease.

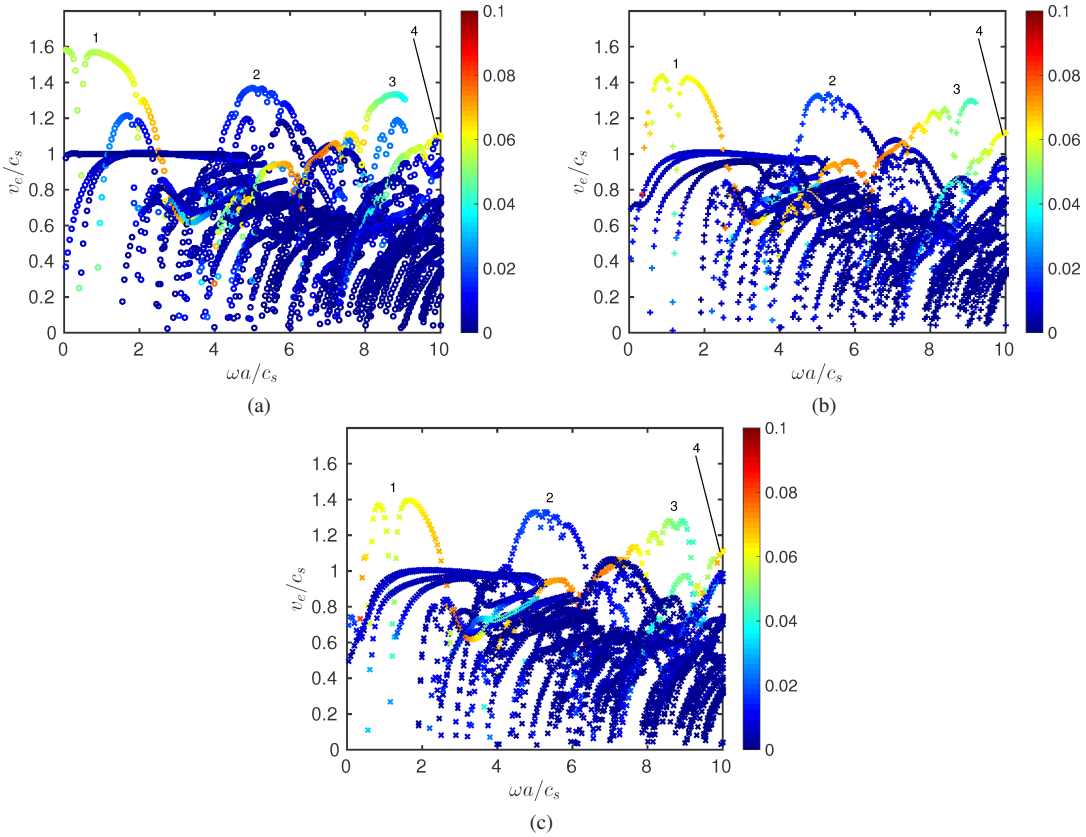

Figure 12: High-frequency energy velocity dispersion curves for a seven-wire strand with material damping computed with the reduced model: (a) $n = 0$, (b) $n = +1$, (c) $n = -1$. Color: modal amplitude $\sqrt{N}|\alpha|$ for an excitation localized inside a peripheral wire (color online).

6. Conclusion

In this paper, a waveguide formulation has been presented to account for the discrete rotational symmetry of the cross-section of elastic waveguides. Both the free and the forced response problems have been considered. To circumvent a loss of symmetry in the eigenproblem, a specific biorthogonality relationship has been derived. This relation can be interpreted as a discrete version of Auld's real biorthogonality relationship. It allows an explicit calculation of modal coefficients of the forced response written as a modal expansion, without solving left eigenproblems. The solution remains applicable to non-propagating modes, fully anisotropic materials and lossy waveguides.

The method has been tested for the simple example of a cylinder and for the more complex test case of a seven-wire strand. Both reductions in terms of dofs and modes significantly contribute to diminishing the computational effort. Besides, the rotationally symmetric formulation naturally provides a classification of modes in terms of their circumferential order, which can be of great help for the dynamic analysis of complex structures. This formulation opens new possibilities for the numerical analysis of complex waveguides in high-frequency regime. For instance, it could facilitate the analysis of cables having a more complex architecture than seven-wire strands and involving rotational symmetry of higher order.

Acknowledgements

The author wishes to thank Région Pays de la Loire and the West Atlantic Marine Energy Center for their financial support.

Appendix A. Circumferential order decomposition of elastodynamic fields

The sum of the first N terms of a geometric series is:

$$\sum_{s=0}^{N-1} r^s = \begin{cases} \frac{1-r^N}{1-r} & \text{if } r \neq 1 \\ N & \text{if } r = 1 \end{cases} \tag{A.1}$$

where r denotes the common ratio. Setting $r = \mathrm{e}^{\mathrm{i}2\pi(s'-s)/N}$, one gets the following useful formula:

$$\frac{1}{N}\sum_{s=0}^{N-1} \mathrm{e}^{\mathrm{i}2\pi(n-n')s/N} = \begin{cases} 0 & \text{if } n' \neq n \\ 1 & \text{if } n' = n \end{cases} \tag{A.2}$$

where n' belongs to the same integer space as n (see Eq. (13)).

Let us now consider the elastodynamic field of cell s, denoted by ${}^s\phi$. We can write the following decomposition:

$${}^s\phi = \sum_n \phi^{(n)} \mathrm{e}^{\mathrm{i}2\pi ns/N} \tag{A.3}$$

Multiplying both sides by $\mathrm{e}^{-\mathrm{i}2\pi n's/N}$ and summing over every cell s yields:

$$\sum_{s=0}^{N-1} {}^s\phi \mathrm{e}^{-\mathrm{i}2\pi n's/N} = \sum_n \left(\phi^{(n)} \sum_{s=0}^{N-1} \mathrm{e}^{\mathrm{i}2\pi(n-n')s/N} \right) \tag{A.4}$$

Using the formula (A.2), one finally gets the nth coefficient of the decomposition:

$$\phi^{(n)} = \frac{1}{N}\sum_{s=0}^{N-1} {}^s\phi \mathrm{e}^{-\mathrm{i}2\pi ns/N} \tag{A.5}$$

Noticing that $\frac{2\pi s}{N} \xrightarrow{N\to\infty} \theta$, the degeneracy of Eqs. (A.3) and (A.5) as the number of cells goes to infinity yields:

$${}^s\phi \xrightarrow{N\to\infty} \phi(\theta) = \sum_{n=-\infty}^{+\infty} \phi^{(n)} \mathrm{e}^{\mathrm{i}n\theta}, \quad \phi^{(n)} \xrightarrow{N\to\infty} \frac{1}{2\pi}\int_{-\pi}^{+\pi} \phi(\theta)\mathrm{e}^{-\mathrm{i}n\theta}\mathrm{d}\theta \tag{A.6}$$

which are the well-known Fourier series formula. The results presented in this paper actually degenerate to the axisymmetry case (*i.e.* continuous rotational symmetry). It can be checked that the biorthogonality (28) and the solution given by Eqs. (46) and (45) remain applicable to a fully axisymmetric waveguide formulation (although the expressions of the elementary matrices (5) are different in this case – see for instance Ref. [22] for these expressions).

References

[1] P. Wilcox, M. Evans, O. Diligent, P. Cawley, Dispersion and excitability of guided acoustic waves in isotropic beams with arbitrary cross-section, in: D. O. Thompson, D. E. Chimenti (Eds.), Review of Progress in Quantitative NDE, Vol. 615, AIP Conference Proceedings, New York, 2002, pp. 203–210.

[2] A. Velichko, P. D. Wilcox, Modeling the excitation of guided waves in generally anisotropic multilayered media, Journal of the Acoustical Society of America 121 (2007) 60–69.

[3] W. T. Thomson, Transmission of elastic waves through a stratified solid medium, J. Appl. Phys. 21 (1950) 89–93.

[4] N. A. Haskell, The dispersion of surface waves on multilayered media, Bull. Seismol. Soc. Am. 43 (1953) 17–34.

[5] E. Kausel, J. Roësset, Stiffness matrices for layered soils, Bull. Seismol. Soc. Am. 71 (1981) 1743–1761.

[6] B. N. Pavlakovic, M. J. S. Lowe, D. N. Alleyne, P. Cawley, Disperse: A general purpose program for creating dispersion curves, in: Review of Progress in Quantitative NDE, Vol. 16, 1997, pp. 185–192.

[7] L. Gry, C. Gontier, Dynamic modelling of railway track : A periodic model base on a generalized beam formulation, Journal of Sound and Vibration 199 (1997) 531–558.

[8] B. R. Mace, D. Duhamel, M. J. Brennan, L. Hinke, Finite element prediction of wave motion in structural waveguides, The Journal of the Acoustical Society of America 117 (2005) 2835–2843.

[9] D. Duhamel, B. R. Mace, M. J. Brennan, Finite element analysis of the vibrations of waveguides and periodic structures, Journal of Sound and Vibration 294 (2006) 205–220.

[10] F. Treyssède, Numerical investigation of elastic modes of propagation in helical waveguides, The Journal of the Acoustical Society of America 121 (2007) 3398–408.

[11] R. Nelson, S. Dong, R. Kalra, Vibrations and waves in laminated orthotropic circular cylinders, J. Sound Vib. 18 (1971) 429–444.

[12] E. Kausel, An explicit solution for the Green functions for dynamic loads in layered media, MIT Research Report R81-13, Department of Civil Engineering, School of Engineering, Massachusetts Institute of Technology, 1981.

[13] G. Liu, J. Achenbach, Strip element method to analyze wave scattering by cracks in anisotropic laminated plates, J. Appl. Mech. 62 (1995) 607–607.

[14] T. Hayashi, W.-J. Song, J. L. Rose, Guided wave dispersion curves for a bar with an arbitrary cross-section, a rod and rail example, Ultrasonics 41 (2003) 175–183.

[15] I. Bartoli, A. Marzani, F. Lanza di Scalea, E. Viola, Modeling wave propagation in damped waveguides of arbitrary cross-section, Journal of Sound and Vibration 295 (2006) 685–707.

[16] H. Gravenkamp, H. Man, C. Song, J. Prager, The computation of dispersion relations for three-dimensional elastic waveguides using the scaled boundary finite element method, J. Sound Vib. 332 (2013) 3756–3771.

[17] F. Treyssède, Spectral element computation of high frequency leaky modes in three-dimensional solid waveguides, Journal of Computational Physics 314 (2016) 341–354.

[18] F. Treyssède, Dispersion curve veering of longitudinal guided waves propagating inside prestressed seven-wire strands, Journal of Sound and Vibration 367 (2016) 56–68.

[19] F. Maurin, C. Claeys, L. Van Belle, W. Desmet, Bloch theorem with revised boundary conditions applied to glide, screw and rotational symmetric structures, Computer Methods in Applied Mechanics and Engineering 318 (2017) 497–513.

[20] E. Manconi, B. R. Mace, Wave characterization of cylindrical and curved panels using a finite element method, The Journal of the Acoustical Society of America 125 (2009) 154–163.

[21] J. M. Renno, B. R. Mace, Calculating the forced response of cylinders and cylindrical shells using the wave and finite element method, Journal of Sound and Vibration 333 (2014) 5340–5355.

[22] A. Marzani, Time-transient response for ultrasonic guided waves propagating in damped cylinders, International Journal of Solids and Structures 45 (2008) 6347–6368.

[23] H. Gravenkamp, C. Birk, C. Song, The computation of dispersion relations for axisymmetric waveguides using the scaled boundary finite element method, Ultrasonics 54 (2014) 1373–1385.

[24] D. L. Thomas, Dynamics of rotationally periodic structures, International Journal for Numerical Methods in Engineering 14 (1979) 81–102.

[25] M. Petyt, Introduction to Finite Element Vibration Analysis, Cambridge University Press, 1990.

[26] F. Treyssède, L. Laguerre, Numerical and analytical calculation of modal excitability for elastic wave generation in lossy waveguides, Journal of the Acoustical Society of America 133 (2013) 3287–3837.

[27] F. Tisseur, K. Meerbergen, The quadratic eigenvalue problem, SIAM Review 43 (2001) 235–286.

[28] R. Lehoucq, D. Sorensen, C. Yang, ARPACK User's Guide: Solution of Large Scale Eigenvalue Problems with Implicitly Restarted Arnoldi Methods, SIAM, Philadelphia, PA, 1998.

[29] B. A. Auld, Acoustic Fields and Waves in Solids, 2nd Edition, Vol. II, Krieger, Malabar, FL, 1990, 432 p.

[30] D. J. Mead, A general theory of harmonic wave propagation in linear periodic systems with multiple coupling, Journal of Sound and Vibration 27 (1973) 235–260.

[31] R. S. Langley, A variational principle for periodic structures, Journal of Sound and Vibration 135 (1989) 135–142.

[32] J. D. Achenbach, Reciprocity in elastodynamics, Cambridge University Press, Cambridge, UK, 2003, 255 p.

[33] F. Treyssède, L. Laguerre, Investigation of elastic modes propagating in multi-wire helical waveguides, Journal of Sound and Vibration 329 (10) (2010) 1702–1716.

[34] C. Geuzaine, J.-F. Remacle, Gmsh: a three-dimensional finite element mesh generator with built-in pre- and post-processing facilities, International Journal for Numerical Methods in Engineering 79 (2009) 1309–1331.
[35] Three-dimensional modeling of elastic guided waves excited by arbitrary sources in viscoelastic multilayered plates, Wave Motion 52 (2015) 33–53.
[36] W. B. Fraser, Othogonality relation for rayleigh-lamb modes of vibration of a plate, Journal of the Acoustical Society of America 59 (1976) 215–216.
[37] V. Pagneux, A. Maurel, Lamb wave propagation in elastic waveguides with variable thickness, Proceedings of the Royal Society A 462 (2006) 1315–1339.
[38] A. Frikha, P. Cartraud, F. Treyssède, Mechanical modeling of helical structures accounting for translational invariance. Part 1: Static behavior, International Journal of Solids and Structure 50 (2013) 1373–1382.
[39] F. Treyssède, A. Frikha, P. Cartraud, Mechanical modeling of helical structures accounting for translational invariance. Part 2: Guided wave propagation under axial loads, International Journal of Solids and Structure 50 (2013) 1383–1393.
[40] F. Treyssède, Investigation of the interwire energy transfer of elastic guided waves inside prestressed cables, Journal of Acoustical Society of America 140 (2016) 498–509.
[41] A. Nawrocki, M. Labrosse, A finite element model for simple straight wire rope strands, Computers & Structures 77 (2000) 345–359.
[42] F. Maurin, Bloch theorem with revised boundary conditions applied to glide and screw symmetric, quasi-one dimensional structures, Wave Motion 61 (2016) 20–39.
[43] B. N. Pavlakovic, M. J. S. Lowe, P. Cawley, High-frequency low-loss ultrasonic modes in imbedded bars, Journal of Applied Mechanics 68 (2001) 67.